

Reverberation Mapping and the Disk Wind Model of the Broad Line Region

J. Chiang and N. Murray

Canadian Institute for Theoretical Astrophysics, McLennan Labs, 60 St. George Street, Toronto,
Ontario, Canada, M5S 1A1

ABSTRACT

Using the disk wind model of Murray et al. (1995), we calculate line profiles and frequency-resolved response functions for broad line emission from the surface of an accretion disk in an AGN in the presence of a radiatively driven wind. We find that the combined effects of the shears in the wind and in the disk itself produce anisotropic line emission which solves several well-known problems connected with disk models of the broad line region. In particular, the broadening of resonance lines such as CIV, Ly α , and NV can be attributed to orbital motion of the disk gas at radii as close as $\sim 10^{16}$ cm in Seyferts without requiring unrealistically large emission regions in order to produce single-peaked profiles. Furthermore, the anisotropy of the line emission results in frequency-dependent response functions which are no longer red-blue symmetric so that the time delays inferred for the various red and blue components of the line agree qualitatively with recent reverberation mapping observations of NGC 5548.

Subject headings: galaxies: active — broad emission lines: observations — quasars: general

1. Introduction

Broad emission lines (BELs) are the distinguishing feature of AGN spectra; and the variability, absorption, profile shape and strength of these lines are our most powerful probes of the inner structure of active galactic nuclei. The basic photoionization model and the evidence for variability in the both the lines and continuum fluxes of AGNs led Blandford & McKee (1982) to propose “reverberation mapping” as a means of constraining the geometry and kinematics of the Broad Line Region (BLR). The principle underlying reverberation mapping is that the light curve of a given line, $L(t)$, can be related to the continuum light curve, $C(t)$, by a causal, linear transformation. The frequency-dependent version of this transformation is

$$L(t, \nu) = \int_0^{+\infty} \psi(\tau, \nu) C(t - \tau) d\tau, \quad (1)$$

where the transfer function $\psi(\tau, \nu)$ is the emission line response to a δ -function outburst of the ionizing continuum. In principle, the convolution theorem and Fourier inversion can be used to

determine $\psi(\tau, \nu)$ from data. The actual geometry and velocity structure of the BLR can then be inferred from some model for the kinematics of the BLR and the fact that the surfaces of constant delay are paraboloids aligned along the observer line-of-sight with the central continuum source at the foci.

The difficulties associated with actually performing such an inversion have motivated long-term observations of AGN in order to obtain high quality spectra and light curves. The first of these extensive monitoring programs was the combined IUE (International Ultraviolet Explorer)/ground-based observations of NGC 5548 in 1988-89 (Clavel et al. 1991). Several major insights into the BLR resulted from the analysis of these NGC 5548 observations. First of all, the size of the BLR was found to be substantially smaller than the size indicated by photoionization calculations of cloud models of the BLR (Krolik et al 1991). Furthermore, cross-correlation analysis of light curves of various lines with the continuum has shown that the BLR is stratified: longer lag times were found for lower ionization lines such as $H\beta$ and $CIII]$ than for higher ionization lines such as NV , CIV and $HeII$ (Krolik et al. 1991). Also, because of the higher quality spectral data, the response functions of separate components of a single line could be studied. Crenshaw & Blackwell (1990) found evidence for a faster response from the red-shifted half of the CIV line versus the blue-shifted half. The complexity of the BLR which these studies revealed called for even better data.

The recent HST/IUE/ground-based effort to monitor NGC 5548 (Korista et al. 1995; hereafter K95) has produced the highest quality data yet obtained for probing the BLR via reverberation mapping techniques. K95 have confirmed the difference between the red-shifted and blue-shifted responses of the CIV line. They have also provided better constraints on the ionization stratification for some of the higher ionization state lines.

The most direct evidence of these effects has been obtained by examining the cross-correlation of the emission line light curves with the continuum. Recently, efforts have been made towards deconvolutions of the actual line response functions using various techniques (Horne 1994; Pijpers 1994; Krolik & Done 1995). Underscoring the importance of modeling, “echo images” in the τ - ν plane for various models of the broad line region (including Keplerian disks and spherically symmetric models with radial infall or out-flow) have been produced, anticipating frequency-resolved response function deconvolutions (Welsh & Horne 1991; Perez, Robinson, & de la Fuente 1992). Done & Krolik (1995) and Wanders et al. (1995) have made the first attempts at such a deconvolution for the CIV line of NGC 5548. Following K95, they divided the line into four frequency bands—two “core” components and two “wing” components; they derived separate response functions for each, confirming the results of the cross-correlation results of K95, and were able to study specific BLR models in greater detail.

Current thinking about the BLR has been dominated for the past decade by the cloud picture (see Peterson 1994 for a review). In these models, dense clouds appropriately distributed in velocity are photoionized by the central continuum and emit the line photons which form the

broad lines. Since there is very little agreement about how such clouds are formed, how they are confined, and how they attain their velocity distribution, cloud models have the advantage of considerable flexibility in describing the observations. Reverberation mapping and photoionization models have placed some constraints on the nature of the BEL cloud region: the characteristic radius of the BLR is likely $\sim 3\text{-}10$ lt-days; the clouds are almost certainly optically thick, though the absence of Lyman edges suggests that individual clouds are significantly smaller than the size of the central continuum emitting region; the smoothness of the line profiles implies that there are of order $> 10^5$ clouds contributing to any given line profile. Furthermore, if the clouds are distributed spherically or nearly so, then the tendency for non-zero lags in the line response implies that the cloud emission is anisotropic, with the emission directed primarily towards the central source. This is consistent with the clouds being optically thick, and Ferland et al. (1992) have performed photoionization calculations to determine the expected emission profile for such clouds. Finally, the faster response times for the red wing of the CIV line of NGC 5548 versus the blue wing imply that any radial motion which the clouds possess must be predominantly inward rather than away from the central source.

It is this last feature which has led some to dismiss the disk model of the BLR. Because the velocity field in a disk, which is usually taken to be Keplerian, is symmetric with respect to red and blue shifted emission, it is expected that the timing response for both sides of the line should also symmetric (Done & Krolik 1995). However, this is only necessarily the case if the line emission from the surface of the disk is *isotropic* as is generally assumed (Welsh & Horne 1991; Dumont et al. 1990; Blandford & McKee 1982). In this work, we show that in the disk wind model of Murray et al. (1995; hereafter M95) the combination of the shears in a Keplerian disk and a radiatively driven disk wind produces an anisotropic opacity for the line emission. This emission anisotropy has several important consequences: it solves the double-peak problem of disk line profiles (Mathews 1982) without requiring unrealistically large BLR radii; it provides a natural explanation for the faster response of the red-shifted line emission despite the symmetry in the disk velocity structure; and it establishes a connection with the observed blueshifted absorption in the CIV line of NGC 5548 and the disk wind models of Broad Absorption Line QSOs. Furthermore, this model for the broad line region allows the mass of the central object to be constrained, and thus provides additional evidence for the massive black hole hypothesis for the centers of active galactic nuclei.

The plan for the remainder of this paper is as follows: In § 2, we review the disk wind model of M95, discuss its observational connection with warm absorbers and Seyfert galaxies, derive the expressions for computing time-averaged line profiles, and compare a model line profile with data from NGC 5548. In § 3, we derive the frequency-resolved response functions, discuss how the red/blue timing asymmetry arises, apply our calculations to the NGC 5548 data and compare our results with the deconvolved response functions of Done & Krolik (1995) and Wanders et al. (1995). In § 4, we discuss some observational consequences of our model, address possible objections and discuss prospects for more detailed work in the future. Finally, we summarize our

conclusions in § 5.

2. The Disk Wind Model

Our model for the BEL region of AGNs is based upon the Broad Absorption Line (BAL) QSO Model of M95. In BALQSOs, the broad line spectra are similar to that of ordinary QSOs except for the deep, broad absorption troughs blueward of line center. Based on this similarity, Weymann et al. (1991) have concluded that ordinary QSOs and BALQSOs belong to the same class of object—only the observer’s line-of-sight to the central source distinguishes them, passing through absorbing material for the latter objects. Because some of the line emission is also absorbed, the cloud picture requires that two distinct sets of clouds exist in the broad line region. The broad emission line clouds exist at the inner radii, closer to the central continuum, while the broad absorption line clouds surround them, with appropriate covering factor to allow the absorption line emission.¹

The complexities and difficulties associated with cloud models of BALQSOs led M95 to consider a different approach. Noting the similarity in the BAL profiles to the P-Cygni profiles found in O star spectra, they considered the possibility that a radiatively driven wind provides the observed absorption. In O stars, it has been well established that such winds are responsible for the shape of the resonance lines (Castor, Abbott & Klein 1975; Pauldrach et al. 1994). Following the formalism of Castor et al. (1975) for radiatively driven winds, M95 calculated the dynamics of a wind which is driven from the surface of an accretion disk. They found that the velocity and ionization structure of these winds can account for the width and shape of the absorption troughs as well as providing a natural explanation of the inferred covering factor ($\sim 10\%$) of the BAL region. The relevance of this model for lower luminosity AGN became clearer when a connection was established between the discovery in X-rays of photoionized bulk outflows, the so-called “warm absorbers” (Turner et al. 1993; Mathur et al. 1994), in Seyfert galaxies, and the presence of blueward absorption features in resonance line spectra in these same objects (Murray & Chiang 1995a). These results suggest that radiatively driven winds may be a ubiquitous feature of all AGN. Since broad emission lines are also universal, it is natural that a connection exists between them as well.

In order to illustrate the applicability of the disk wind model to the broad emission line region, we consider a simplified description of the velocity structure of the wind. The wind consists of nearly radial streamlines which have footpoints at various radii on the surface of the disk. Near the footpoint radius, r_f , for a given streamline, the gas is initially driven upwards by the surface radiation of the disk. At a vertical height which is approximately the scale height of the disk,

¹Various descriptions of cloud models for BEL and BAL regions can be found in Arav et al. (1994); Emmering, Blandford, & Schlossman (1992) and references therein.

the radiation pressure from the central continuum source becomes strong enough to push the gas predominantly radially outwards. M95 have integrated the equations of motion using the radiation force law determined from calculations using the photoionization code CLOUDY (Ferland 1993) and the line list of Verner, Barthel, & Tytler (1994). They found that the radial component of the gas velocity along a streamline can be described approximately by

$$v_r(r) = v_\infty \left(1 - \frac{r_f}{r}\right)^\gamma, \quad (2)$$

where the terminal velocity of the streamline, v_∞ , is within factors of order unity of the local escape velocity, $v_{\text{esc}} = \sqrt{2GM/r_f}$, and the exponent $\gamma \simeq 1.0\text{-}1.3$. It should be noted that this exponent differs from the result for O stars ($\gamma \simeq 0.5$, Castor et al. 1975) because of the differing force multiplier law, as derived from the photoionization calculations, and the importance of the centrifugal support of the rotating Keplerian disk. In the following discussion, we will use $\gamma = 1$.

M95 have performed dynamical and photoionization calculations which show that the inner edge of the wind should be located at $\sim 3 \times 10^{15}$ cm for an accretion disk around a $10^7 M_\odot$ black hole. It is important to note that at these radii, the shear in the disk itself is sufficient to make the Sobolev approximation an appropriate description of the resonance line transfer in the disk (cf Castor 1970). Murray & Chiang (1995b) discuss the validity of this approximation in greater detail. For our purposes, it is sufficient to note that the Sobolev length scale associated with the shear due to the differential rotation of the disk is

$$l_S \sim \frac{v_{\text{th}}}{v_\phi/r} \sim 10^{10} \text{ cm}, \quad (3)$$

where $v_{\text{th}} \sim 10^6 \text{ cm s}^{-1}$ is the thermal velocity of the disk gas, and $v_\phi = \sqrt{GM/r}$ is the azimuthal disk velocity. This length is much smaller than the length scale of the Shakura-Sunyaev (1973) thin-disk solution of $\sim 10^{13}$ cm for a $10^7 M_\odot$ black hole; this implies that, as within the wind itself, the Sobolev approximation also applies to the disk.

We expect that the largest contribution to the line emission will be from regions of high density. Therefore, we will assume for now that the line emission originates primarily near the wind footpoints at the surface of the accretion disk where the densities are high ($n_H \sim 10^9 \text{ cm}^{-3}$), but the continuum optical depths, which are largely due to electron scattering, are still no more than order unity. At these locations, the velocity of the gas is composed of a radial component due to the wind and an azimuthal component due to the disk motion:

$$\vec{v} = v_r \hat{r} + v_\phi \hat{\phi}. \quad (4)$$

For an observer located in the y - z plane with a line-of-sight angle i with respect to the disk symmetry axis (see Figure 1), the projected velocity shift at a location (r, ϕ) on the disk is

$$v_{\text{proj}} = \sin i (v_r \sin \phi + v_\phi \cos \phi). \quad (5)$$

Note that we have neglected the finite thickness of the disk ($\sim 10^{13}$ cm) which is much smaller than the inferred radius of the BLR ($\sim 10^{16}$ cm).

Because of the azimuthal symmetry of the problem, we model the line source function, $S(r)$, to be a function only of the disk radius. The contribution to the line profile at a given frequency is

$$L_\nu = \cos i \int_{r_{\min}}^{r_{\max}} r dr \int_0^{2\pi} d\phi k(r) S(r) \frac{1 - e^{-\tau}}{\tau} \delta(\nu - \tilde{\nu}(\phi, r)), \quad (6)$$

where r_{\min} and r_{\max} are the radial boundaries of the BLR, $\tilde{\nu}$ is the Doppler-shifted frequency of the line at the disk element which has velocity v_{proj} :

$$\tilde{\nu} = \nu_0 \left(1 + \frac{v_{\text{proj}}}{c} \right) \quad (7)$$

and ν_0 is the frequency of the line. The optical depth τ is angle dependent and is *locally* determined in the Sobolev approximation, and $k(r)$ is the integrated line opacity (Rybicki & Hummer 1983). In the notation of Hamann, Korista & Morris (1993) the quantity

$$\beta(r, \phi, i) = \frac{1 - e^{-\tau}}{\tau} \quad (8)$$

is known as the *directional* escape probability. Transforming the δ -function and evaluating the ϕ -integral, we obtain for the integrand of Equation 6

$$\frac{dL_\nu}{dr} = r k(r) S(r) \cos i \left| \frac{d\tilde{\nu}}{d\phi} \right|^{-1} \beta(r, \phi, i) \quad (9)$$

$$= \frac{c}{\nu_0 \tan i |v_r \cos \phi - v_\phi \sin \phi|} r k(r) S(r) \beta(r, \phi, i) \quad (10)$$

where ϕ satisfies $\tilde{\nu}(r, \phi) = \nu$ for a given radius r .

The line optical depth in the Sobolev approximation is

$$\tau = \frac{\kappa \rho v_{\text{th}}}{|\hat{n} \cdot \Lambda \cdot \hat{n}|}, \quad (11)$$

where κ is the line absorption coefficient, ρ is the density, \hat{n} is the line-of-sight vector to the observer and Λ is the symmetric strain tensor (Castor 1970; Rybicki & Hummer 1978). For the CIV line, the line absorption coefficient is

$$\kappa \simeq 2.61 \times 10^7 \eta_{\text{C}^{+3}} \quad (12)$$

assuming a cosmic abundance of carbon and where $\eta_{\text{C}^{+3}}$ is the fractional abundance of the C^{+3} ion. We expect $\eta_{\text{C}^{+3}}$ to be of order unity throughout the CIV BELR. For the velocity structure given by Equations 2 & 4, we have

$$\hat{n} \cdot \Lambda \cdot \hat{n} = \sin^2 i \left[\frac{\partial v_r}{\partial r} \sin^2 \phi + \left(\frac{\partial v_\phi}{\partial r} - \frac{v_\phi}{r} \right) \sin \phi \cos \phi + \frac{v_r}{r} \cos^2 \phi \right] \quad (13)$$

$$= \sin^2 i \left[v_\infty \frac{r_f}{r^2} \sin^2 \phi - \frac{3}{2} \frac{v_\phi}{r} \sin \phi \cos \phi + \frac{v_r}{r} \cos^2 \phi \right]. \quad (14)$$

Evaluated at the high density regions near the footpoints of the wind streamlines, this factor is of order $\sim v_\phi/r_f$. Combining Equations 11, 12, and 14, the optical depth in the line is of order

$$\tau \sim 10^5 \frac{n_H}{10^9 \text{cm}^{-3}}; \quad (15)$$

so we can use

$$\beta \simeq \frac{1}{\tau}. \quad (16)$$

The final expression for the luminosity per unit radius is

$$\frac{dL_\nu}{dr} = r S(r) \sin i \cos i \left| \frac{\frac{\partial v_r}{\partial r} \sin^2 \phi - \frac{3}{2} \frac{v_\phi}{r} \sin \phi \cos \phi + \frac{v_r}{r} \cos^2 \phi}{v_r \cos \phi - v_\phi \sin \phi} \right| \quad (17)$$

$$\simeq S(r) \sin i \cos i \left| \left(\frac{v_\infty}{v_\phi} \sin \phi - \frac{3}{2} \cos \phi \right) \right|, \quad (18)$$

where the final form is obtained by evaluating Equation 17 near the wind streamline footpoints, $r \simeq r_f$, and neglecting terms which are proportional to $v_r/v_\phi \lesssim 10^{-2}$. We note that the remaining r -dependence is contained in the source function $S(r)$ given that v_∞ and v_ϕ both scale as $\sim r^{-1/2}$.

It is not entirely clear how the central continuum source illuminates the outer regions of the disk where the broad emission lines are formed. The standard picture of AGNs is that the UV and X-ray continuum emission is emitted from the hot inner regions of the accretion disk. However, the Shakura-Sunyaev thin disk solution, which is thought to apply to these inner regions, gives a disk height which is essentially constant from the hot inner regions out to the disk BLR. Therefore, in the standard thin-disk solution, there would not be any lines-of-sight from the continuum source to the BLR.

However, in disk models of the BLR, it is conventional to assume that either that a continuum source exists a moderate distance above the inner regions of the disk (Matt, Fabian & Ross 1993) or that there is a hot, spherical region at the center of the disk (Rokaki & Magnan 1994). Murray & Chiang (1995b) propose a physical explanation for the latter case wherein resonance line pressure makes an additional contribution to the opacity at the inner regions of the disk causing it to “puff up.” In any case, for the purposes of the reverberation mapping study, we will assume that there is a central source of ionizing continuum which is situated not far above the disk plane ($z \sim 10^{13}(M/10^7 M_\odot)$ cm), and which can illuminate the disk BLR.

In order to reproduce a reasonable line profile shape (cf Figure 2), we have found that the radial dependence in Equation 18 can be adequately modeled by

$$S(r) \propto r^{-\alpha}, \quad (19)$$

with a value of $\alpha \simeq 1$. The inner radial boundary of the BLR, r_{\min} , is constrained by the reverberation mapping results and photoionization calculations. The outer radial boundary,

r_{\max} , is determined by the location of the Strömgen radius for the ion in question. Preliminary photoionization results give $r_{\max} \sim 10^2 r_{\min}$ for the CIV line in NGC 5548. Using this radial dependence and these boundaries, we have integrated Equation 6 and find the line profile (solid line) for CIV shown in Figure 2. For comparison, the dashed line is the mean GEX-extracted CIV line profile of NGC 5548 from the recent HST observations (K95) and the dot-dashed line results from the same model calculation except that isotropic emission is assumed. The effect of the anisotropic optical depth is clear: the disk wind shears result in single-peaked profiles, and the shape of the line, except for the blue-ward absorption and a possible contribution from a narrow-line component, are well-matched.

We have used a disk inclination angle $i = 75^\circ$ for this calculation. This choice is motivated by the presence of the warm absorber and the expectation that it is due to a highly ionized component of the disk wind which lies in the observer line-of-sight (Murray & Chiang 1995a). We note that the value of i and the index of the flux radial dependence given in Equation 19 are correlated: the CIV line will be better fit by values of $\alpha \gtrsim 1$ for smaller values of i . It should also be noted that these results only apply to the *shape* of the line from our model. Accordingly, the model lines shown in Figure 2 are normalized so that their equivalent widths match that of the observed line. More complete photoionization calculations would have to be performed using the detailed disk wind velocity and ionization structure and the actual ionizing continuum of NGC 5548 for a full comparison with the data to be made. The preceding arguments are presented to show that the scalings we have inferred are reasonable and that there is physical motivation for the disk wind model.

3. Disk Wind Response Function

So far, the line profiles we have presented are for a steady continuum source. We now derive the transfer function in order to consider variability. We have

$$\begin{aligned} \psi(\tau, \nu) &= \int_{\text{disk}} dA k(r) S(r) \beta(r, \phi, i) \delta(\tau - \tilde{\tau}(r, \phi)) \delta(\nu - \tilde{\nu}(r, \phi)) \\ &= \int r dr \int d\phi k(r) S(r) \beta(r, \phi, i) \delta(\tau - \tilde{\tau}) \delta(\nu - \tilde{\nu}). \end{aligned} \quad (20)$$

For each point on the disk, (r, ϕ) , there is associated a time-delay and frequency, (τ, ν) . Transforming the integral over the disk area to one over τ and ν , we obtain

$$\psi(\tau, \nu) = \frac{r k(r) S(r) \beta(r, \phi, i)}{\left| \begin{array}{cc} \frac{\partial \tau}{\partial r} \frac{\partial \nu}{\partial \phi} - \frac{\partial \tau}{\partial \phi} \frac{\partial \nu}{\partial r} \end{array} \right|} \Bigg|_{\substack{r=\tilde{r}(\tau, \nu) \\ \phi=\tilde{\phi}(\tau, \nu)}}. \quad (21)$$

The denominator is the Jacobian of the transformation, and the entire expression is evaluated at the corresponding locations $(\tilde{r}, \tilde{\phi})$ on the disk which yield the desired time-delay and frequency.

Figure 3 is an image depicting the value of the transfer function as a function of location on the disk (cf Figure 1). Also plotted are the lines of constant time delay (dashed lines) and the lines of constant frequency (solid lines) to illustrate the mapping from (r, ϕ) to (τ, ν) . The lines of constant time delay are given by the intersection of the constant time delay paraboloids and the disk surface. Near the disk surface, the radial component of the velocity, $v_r \sim 10^7$ cm s⁻¹, is small compared with the azimuthal velocity $v_\phi \sim 10^8$ - 10^9 cm s⁻¹ throughout the BLR. Therefore the projected velocity (cf Equation 5) is approximately

$$v_{\text{proj}} \simeq \sqrt{\frac{GM}{r}} \sin i \cos \phi, \quad (22)$$

so that for a given frequency shift $\Delta\nu$, we have

$$r \simeq \frac{GM \sin^2 i}{v_{\text{proj}}^2} \cos^2 \phi. \quad (23)$$

From this expression, we see that the loci of constant absolute shift $|\Delta\nu|$ look like lobes which are nearly red-blue symmetric.

The red-blue asymmetry of the disk response function can be attributed to the radiative transfer effects due to the radial and azimuthal shear of the disk wind. From Equation 18, we see that the ϕ -dependence of the disk contribution to the line luminosity is

$$\frac{dL_\nu}{dr} \propto \left| \frac{v_\infty}{v_\phi} \sin \phi - \frac{3}{2} \cos \phi \right|. \quad (24)$$

Because $v_\infty \sim v_\phi$ and both are intrinsically positive quantities, the transfer function attains small values near the median angles ($\sim 45^\circ, 270^\circ$) in the upper right and lower left quadrants of the disk as shown in Figure 3. These smaller values of the emission seen by the observer are depicted by the lighter pixels in the image. Figure 4 is an echo-image of the response function in (τ, ν) -space; note the similarities and differences with respect to the echo-image maps for disk BLR models with isotropic emission given in Welsh & Horne (1991) and Perez et al. (1992).

Following K95, we consider the timing response for the blue/red wing and core components of the CIV line. The core components are defined to extend from Doppler shifts of 0 to ± 3000 km/s and the wing components from ± 3000 to 10840 km/s. The small arrows in Figure 2 indicate these boundaries at the corresponding wavelengths. We have integrated Equation 21 over frequency for these four bands and found the response functions shown in Figure 5. As with the response functions found by the deconvolutions (Done & Krolik 1995; Wanders et al. 1995), the core components are nearly identical and are very similar to the blue wing component except at very short time scales, $\lesssim 1$ day. Most significantly, the red wing has significantly stronger response at shorter time scales (~ 1 -4 days) than the other three components. In addition, the secondary peaks found by both Wanders et al. (1995) and Done & Krolik (1995) at delays of 8-15 days are also a natural consequence of the disk model.

The faster response of the red wing can be understood by considering Figure 3. The blue and red wing frequency ranges are bounded by the solid lines, and the 0.5, 5 and 10 day time delay lines are indicated by the dashed lines. Within the earlier region, between 0.5 and 5 days, the red wing response is stronger than the response of the blue wing. This occurs because the locations of weaker emission due to the near cancellation of two ϕ -dependent terms in Equation 24 pass through the blue wing region, but not through the corresponding red wing region. At later times, from 5 to 10 days, the situation is reversed—the line of near cancellation of the ϕ -dependent terms now passes predominantly through the red wing region and does not suppress as much emission in the corresponding blue region. In effect, the response in the blue wing “catches-up” to and surpasses that of the red wing—this is evident in the second peak of the blue wing response function at ~ 8 days. In Figure 4, the difference in the red and blue response functions can also be clearly seen.

In order to underscore the applicability of this model to actual data, we have used the combined IUE/HST spectra of K95 to create light curves for the four line components and cross-correlation functions of these model light curves with the continuum. Figure 6 shows the 1350 Å continuum (mean subtracted) as measured by IUE (SWP) and HST over an ~ 80 day period. The solid line is the interpolated continuum we have used for the convolutions, and Figure 7 shows the resulting light curves for each of the four line components. The earlier response of the red wing relative to the blue wing is clearly evident. Figure 8 shows the cross-correlation functions for these light curves with the interpolated 1350 Å continuum (cf Figure 15 in K95). Table 1 shows lists the peak and centroid values of the inferred lags for each component.

4. Discussion

4.1. Response Function Structure and Line Profile Variations

The detailed structure of the frequency-resolved response functions may also be useful in explaining asymmetries in the broad line profiles as well as long term variability in the line structure. The larger second peak in the blue-wing response at ~ 8 days may either “alias” or “anti-alias” structure present in the continuum light curve into the mean line profile for a typical observation. The result would be line profiles which would be skewed toward either the blue or the red depending on the phase and strength of the continuum light curve variations relative to the time window(s) of the observation. On the other hand, Perry, van Groningen, & Wanders (1994) have shown that the variations seen in the shape of the CIV line of NGC 4151 are preceded by similar continuum light curves. They argue that the changes in the line shape may instead be due to structural changes in the BLR, an extended or anisotropic continuum source, or a significantly larger BLR than that deduced from cross-correlation analysis. In any case, the structure of the response functions will still be reflected in the shape of the emission line in the way we have described. If these other effects are not significant, then examining the line profile

structure and the preceding continuum variations may be an additional means of discriminating between different kinematic models of the BLR.

4.2. Constraints on the Mass of the Central Object

The radial extent of the BLR is determined by the reverberation mapping results, and the velocity field is determined by the width of the resonance lines and the photoionization results for the ionization structure of the disk wind. Thus, the observations essentially fix the quantities r and v_ϕ . The assumption of Keplerian motion relates these two quantities by

$$v_\phi = \sqrt{\frac{GM}{r}}, \quad (25)$$

so that the mass of the central object is actually constrained by these observations. Now, since $M \propto r$ for a fixed line width (i.e. $v_\phi \sim \text{constant}$) and since the lags are related to radii on the disk linearly, $\tau \propto r$, we have

$$M \propto \tau. \quad (26)$$

The lags which we infer from the cross-correlation functions (Figure 8 & Table 1) agree with the values given by K95 to within 20%, and we have determined the mass of the central object of NGC 5548 to be $\simeq 10^8 M_\odot$. Furthermore, for objects with line widths similar to NGC 5548, the observed lags for those lines give a direct measurement of the mass of the central object if this model for the BLR is correct.

4.3. Broad Iron $K\alpha$ Lines

One of the difficulties of this model of the Broad Line Region is that observations of broad, redshifted iron $K\alpha$ lines in Seyfert 1s seem to indicate that the disks are being viewed predominantly face-on with inclinations of $i \sim 20\text{-}30^\circ$. In these objects, the iron emission is believed to originate near the inner edge of the accretion disk at radii $\sim 3R_s$, where R_s is the Schwarzschild radius of the central black hole (Matt et al. 1993). Mushotzky et al. (1995) report that *Ginga* observations of NGC 5548 have found that the equivalent width of the Fe $K\alpha$ line is ~ 150 eV and that this is best fit by disk inclinations of $i \sim 15\text{-}38^\circ$. On the other hand, as Done & Krolik (1995) and Wanders et al. (1995) have pointed out, in order for the response functions of a disk with inner radius $\sim 10^{16}$ cm to peak near zero delay, the disk must be highly inclined.

We do not believe that these observations of the iron $K\alpha$ lines and our disk-model for the UV BLR are irreconcilable. First of all, the timing resolution of the NGC 5548 observations is no better than 1 day, and we can still produce response functions with the peak response at time delays < 1 day for disk inclinations as small as $i \sim 60^\circ$. Secondly, Mushotzky et al. (1995) state that only three of the five parameters—inner and outer radii of the emitting region, initial line

energy, disk inclination, and line flux—which are necessary to describe the iron line are actually constrained by the NGC 5548 data. Thirdly, Tanaka et al. (1995) and Matt et al. (1993) have indicated that the emitting material in the Seyfert 1s may be in a higher ionization state than they have considered and that this can increase the relative yield of Fe K α photons, thus relaxing the constraint on larger inclination angles. Finally, it should be noted that the constraints which are also based on the *shape* of the Fe K α arrived at by Tanaka et al. (1995) for the Seyfert galaxy MCG-6-30-15 are based upon radiative transfer calculations which, to our knowledge, ignore the effect of shears in the disk. We have seen that these effects can have a significant impact on the shape of the emission line (cf Figure 2) and may also affect the amount of line flux which escapes.

4.4. Future Work

We have not presented here a detailed model of the line emission from NGC 5548. The photoionization calculations and our simplified model of the disk wind structure are too crude to be expected to match the observations in detail. Hence, we have not attempted to fit the NGC 5548 light curves of the CIV components. In order for that to be accomplished, photoionization calculations using a more detailed physical model of the disk wind structure must be performed. This will enable us to determine better the radial dependence for the emission from each ion, and also probe for non-linear response of the line emission to the continuum. We would also like to use more realistic velocities and shears in Equation 17, and improve the radiative transfer to take into account possible non-local effects from multiple resonant Sobolev surfaces (Rybicki & Hummer 1978).

5. Conclusions

Despite the incompleteness of this model, we have offered a plausible qualitative explanation of the timing response seen in NGC 5548 using a physically motivated model for the BLR. In particular, the response functions we obtain possess all the features found in the response functions obtained by the deconvolution procedures of Wanders et al. (1995) and Done & Krolik (1995): they peak near zero time delay; the red wing response is stronger than the response of the other components at time delays of ~ 1 -4 days; and the secondary peak at 8-14 days is also reproduced. Furthermore, the line profile which we obtain is single-peaked in agreement with the profiles seen for most broad lines in AGN spectra, and we have shown that by using the width of the line profile and the timing response of the red and blue components that we can estimate the mass of the central black hole—for NGC 5548 we find the mass to be $\sim 10^8 M_{\odot}$.

The most significant finding of this work is that the radiative transfer effects which reproduce the observed line profile and timing response *require* that a wind with large radial shears be present. Therefore, if it is accepted that the broad lines are produced from the surface of a disk,

then something which acts like a radiatively driven wind must exist.

6. Acknowledgements

We would like to thank Kirk Korista for generously supplying us with HST spectra of NGC 5548, and Julian Krolik for providing us with a manuscript of his work in advance of publication. This work was supported by NSERC of Canada and by the Connaught Fund of the University of Toronto.

Table 1: Cross-Correlation Results

Crv component	Disk-Wind Model		HST Observations (K95)	
	Δt_{peak} (days)	$\Delta t_{\text{centroid}}$	Δt_{peak}	$\Delta t_{\text{centroid}}$
Blue wing	7.2	6.0	7.5	8.3
Blue core	5.0	4.3
Red core	4.9	4.3
Red wing	3.6	4.4	3.5	4.3

REFERENCES

- Arav, N., Li, Z., & Begelman, M.C. 1994, ApJ, 432, 62
- Blandford, R. D., & McKee, C. F. 1982, ApJ, 255, 419
- Castor, J. I. 1970, MNRAS, 149, 111
- Castor, J. I., Abbott, D. C., & Klein, R. I. 1975, ApJ, 195, 157
- Clavel, J., et al. 1991, ApJ, 366, 64
- Crenshaw, D. M., & Blackwell, J. H., Jr. 1990, ApJ, 358, L37
- Dumont, A. M., & Collin-Souffrin, S. 1990, A&A, 229, 313
- Done, C., & Krolik, J. H. 1995 ApJ, submitted
- Emmering, R.T., Blandford, R.D., & Schlossman, I. 1992, ApJ, 385, 460
- Ferland, G. J. 1993, University of Kentucky Department of Physics and Astronomy Internal Report
- Ferland, G. J., Peterson, B. M., Horne, K. , Welsh, W. F., & Nahar, S. N. 1992, ApJ, 387, 95
- Hamann, F., Korista, K. T. & Morris, S. L. 1993, ApJ, 415, 541
- Horne, K. 1994, in Reverberation Mapping of the Broad-Line Region in Active Galactic Nuclei, eds. P. M. Gondhalekar, K. Horne, and B. M. Peterson, (ASP: San Francisco) p. 23
- Korista, K., et al. 1995, ApJS, 97, 285 (K95)
- Krolik, J. H., Horne, K., Kallman, T. R., Malkan, M. A., Edelson, R. A., & Kriss, G. A. 1991, ApJ, 371, 541
- Krolik, J. H., & Done, C. 1995, ApJ, in press
- Mathews, W. G. 1982, ApJ, 258, 425
- Mathur, S., Wilkes, B., Elvis, M., & Fiore, F. 1994, ApJ, 434, 493
- Matt, G., Fabian, A. C., & Ross, R. R. 1993, MNRAS, 262, 179
- Murray, N., & Chiang, J. 1995a, ApJ, in press
- Murray, N., & Chiang, J. 1995b, in preparation
- Murray, N., Chiang, J., Grossman, S., & Voit, G. M. 1995 ApJ, 451, 498 (M95)

- Mushotzky, R., Fabian, A. C., Iwasawa, K., Kunieda, H., Matsuoka, M., Nandra, K. & Tanaka, Y. 1995, MNRAS, 272, L9
- Nandra, K., & Pounds, K. A. 1994, MNRAS, 268, 405
- Pauldrach, A.W.A., Kudritzki, R.P., Puls, J., Butler, K., & Hunsinger, J. 1994, A&A, 283, 525
- Perez, E., Robinson, A., & de la Fuente, L. 1992, MNRAS, 256, 103
- Perry, J. J., van Groningen, E., & Wanders, I. 1994, MNRAS, 271, 561
- Peterson, B. M. 1994, in Reverberation Mapping of the Broad-Line Region in Active Galactic Nuclei, eds. P. M. Gondhalekar, K. Horne, and B. M. Peterson, (ASP: San Francisco) p. 1
- Pijpers, F. P. 1994, in Reverberation Mapping of the Broad-Line Region in Active Galactic Nuclei, eds. P. M. Gondhalekar, K. Horne, and B. M. Peterson, (ASP: San Francisco) p. 69
- Rokaki, E. & Magnan, C. 1992, A&A, 261,41
- Rybicki, G. B., & Hummer, D. G. 1978, ApJ, 219, 654
- Shakura, N. I., & Sunyaev, R. A. 1973, A&A, 24, 337
- Tanaka, Y., et al. 1995, Nature, 375, 659
- Turner, T. J., Nandra, K., George, I. M., Fabian, A. C., & Pounds, K. A. 1993, ApJ, 419, 127
- Verner, D. A., Barthel, P. D., & Tytler, D. 1994, A&ASS, 108, 287
- Wanders, I. et al. 1995, ApJ, in press
- Welsh, W. F., & Horne, K. 1991, ApJ, 379, 586
- Weymann, R. J., Morris, S. L., Foltz, C. B., & Hewett, P. C. 1991, ApJ, 373, 23

Fig. 1.— Geometry of the disk broad line region. The angle, i , is the disk inclination relative to the observer. The quantities (r, ϕ) label locations on the disk.

Fig. 2.— Data and model line profiles for the CIV line of NGC 5548. The solid line is the model calculation including the effects of the anisotropic emission. The dashed line is the data from the 1994 HST observations described by Korista et al. 1995. Also shown is the double-peaked profile (dot-dashed) of a model line calculation which assumes isotropic emission. The arrows indicate the boundaries of the various wing and core components.

Fig. 3.— Disk map of the line transfer function ψ . The solid lines are the lines of constant frequency indicating the boundaries of the blue and red wing components. They are at $10,840 \text{ km s}^{-1}$ (right side, inner curve), $3,000 \text{ km s}^{-1}$ (right side, outer curve which extends beyond the plot boundaries), $-3,000 \text{ km s}^{-1}$ (left side, outer curve) and $-10,840 \text{ km s}^{-1}$ (left side, inner curve). The dashed lines are the lines of constant time delay at $\tau = 0.5, 5$ and 10 days.

Fig. 4.— Echo image of the transfer function in (v_{proj}, τ) -space. The dashed lines are the boundaries of the various line components.

Fig. 5.— Model response functions for the various components of the CIV line.

Fig. 6.— The continuum at 1350\AA of NGC 5548. The plotted points are the data as measured by IUE and HST (Korista et al. 1995), and the solid curve is the interpolated function we have used in our cross-correlation analysis.

Fig. 7.— Model light curves of the various components of the CIV line of NGC 5548.

Fig. 8.— Cross-correlation functions for the four components of the CIV line with the 1350 \AA continuum.

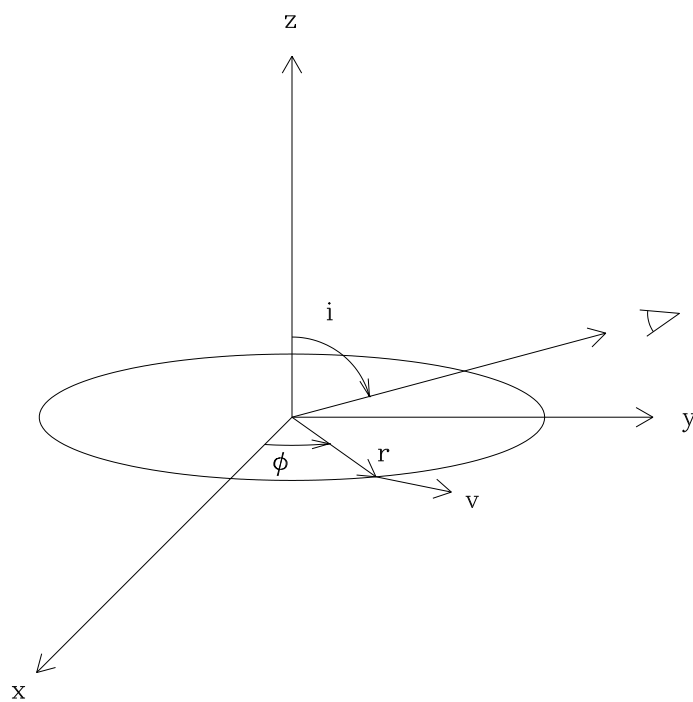


Figure 1

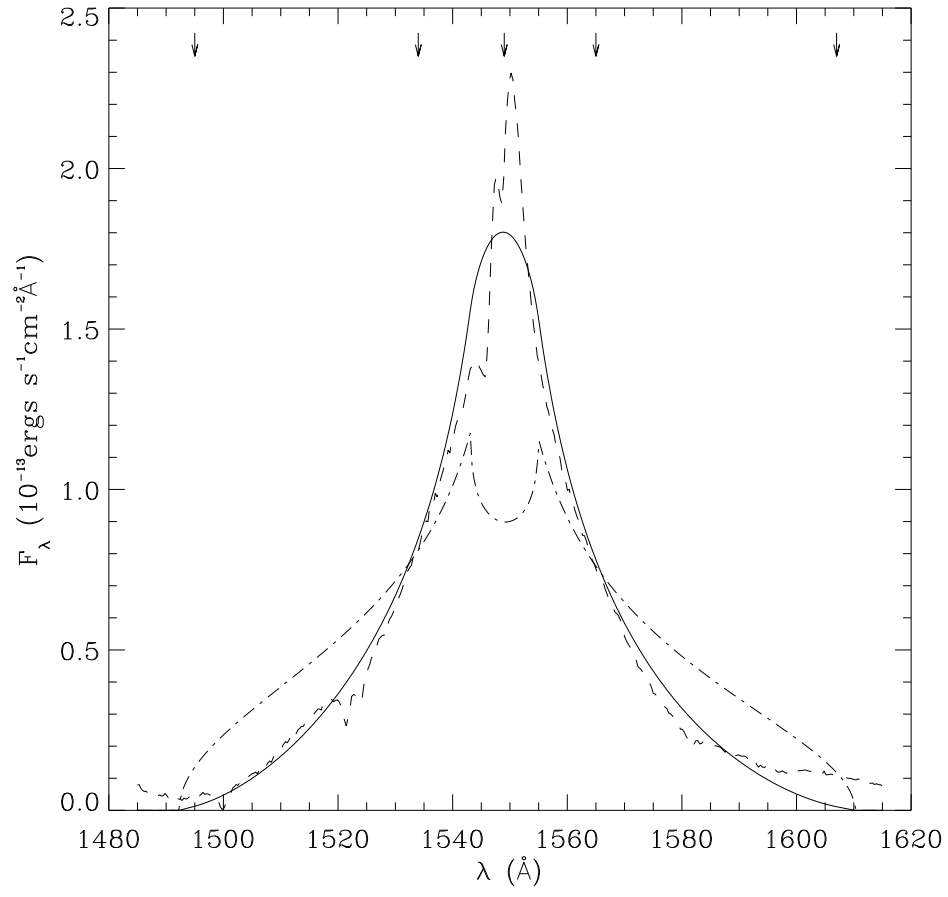


Figure 2

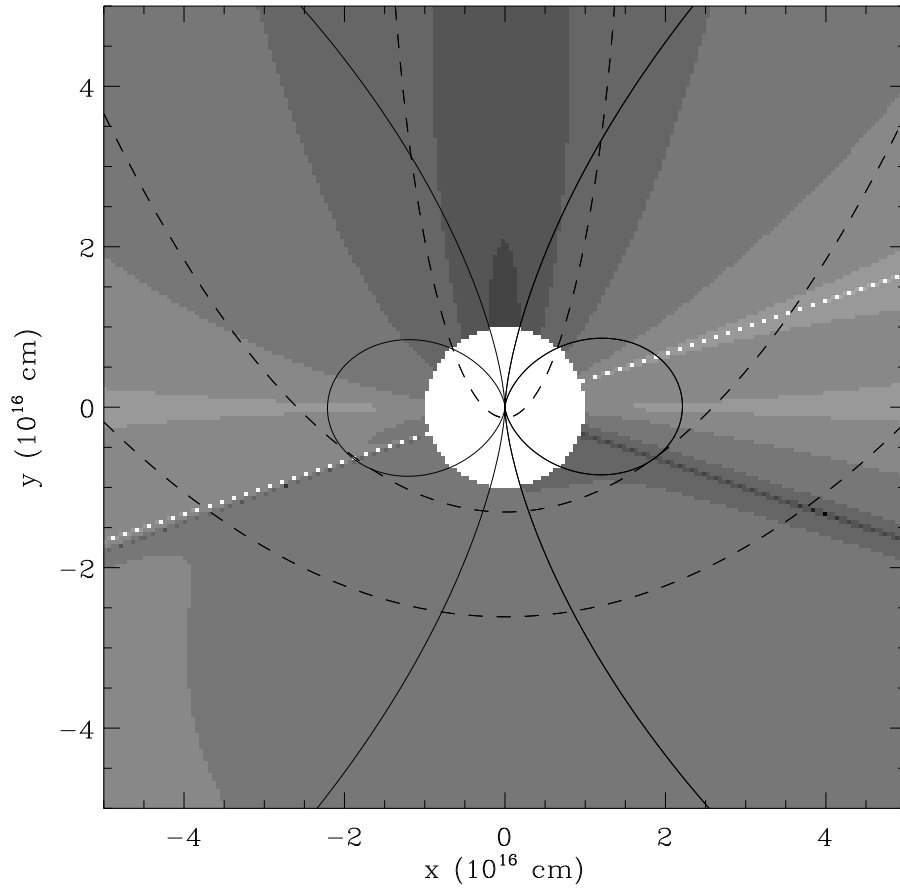


Figure 3

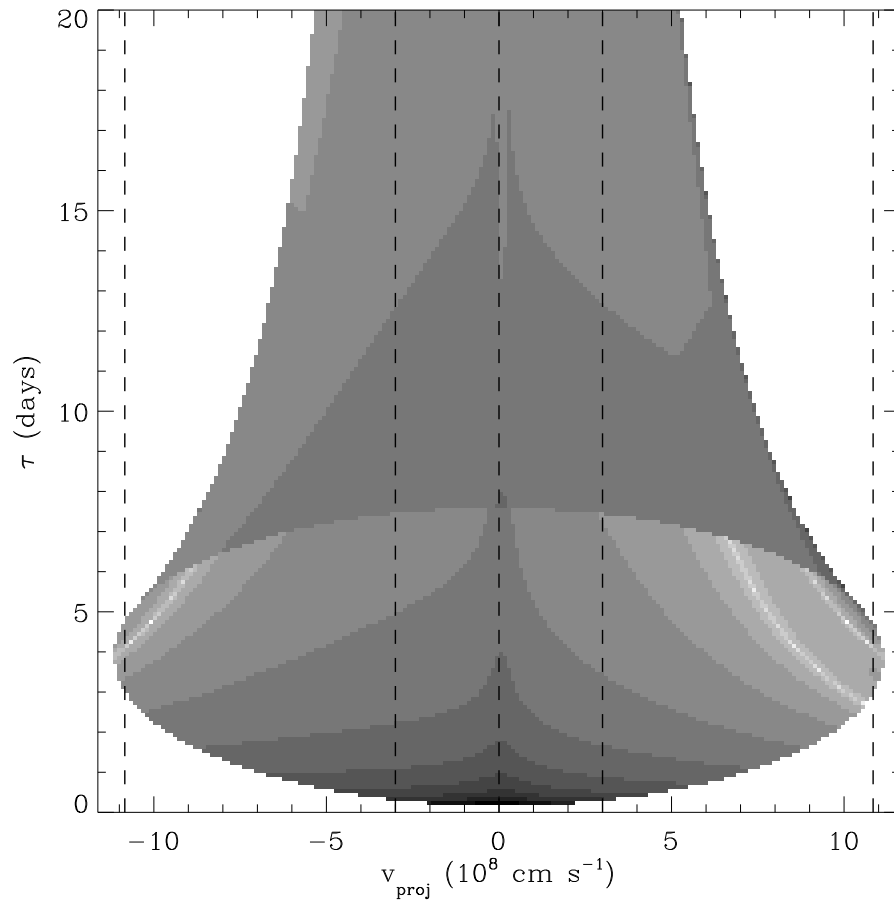


Figure 4

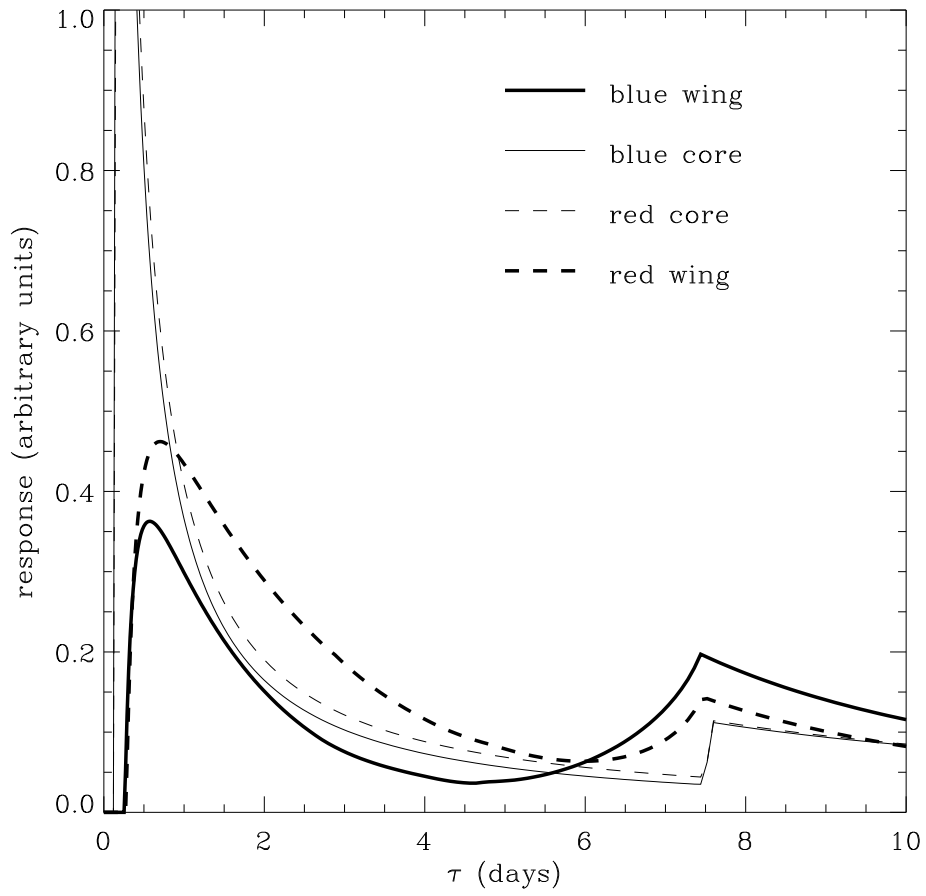


Figure 5

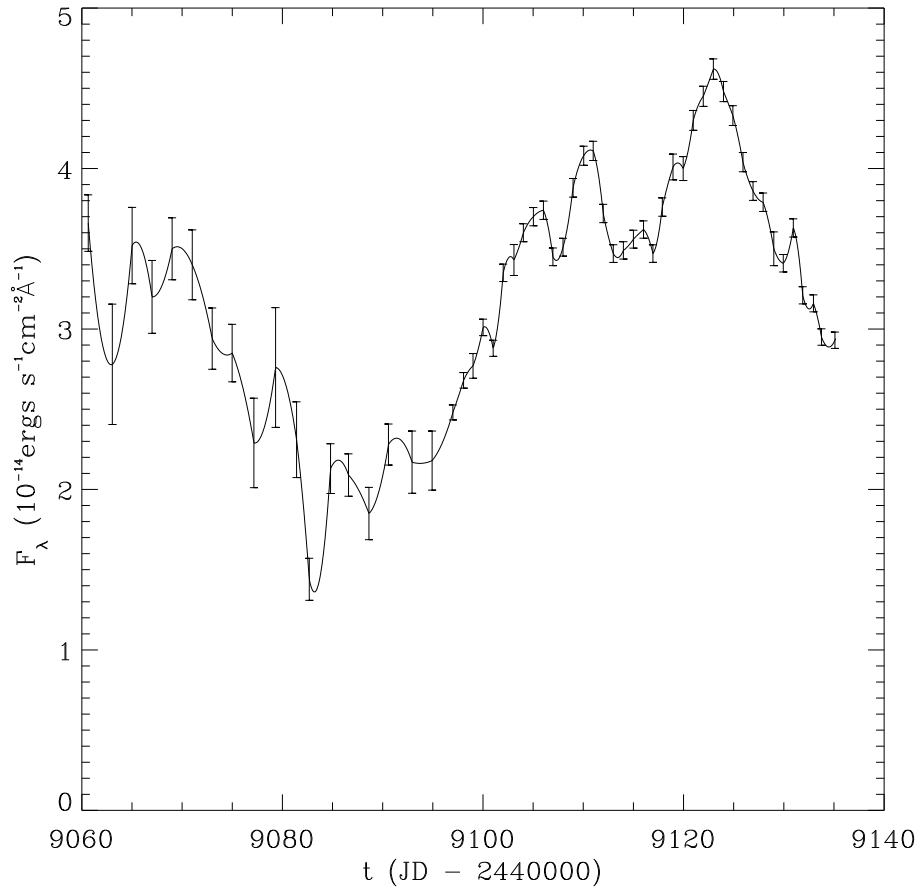


Figure 6

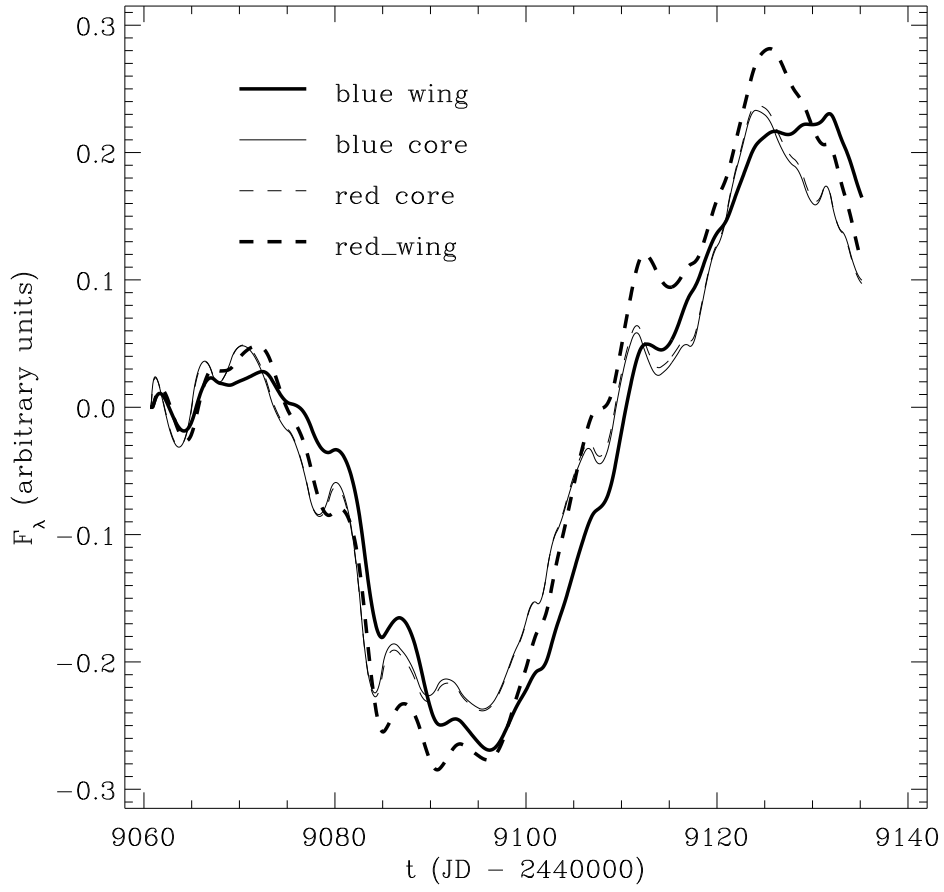


Figure 7

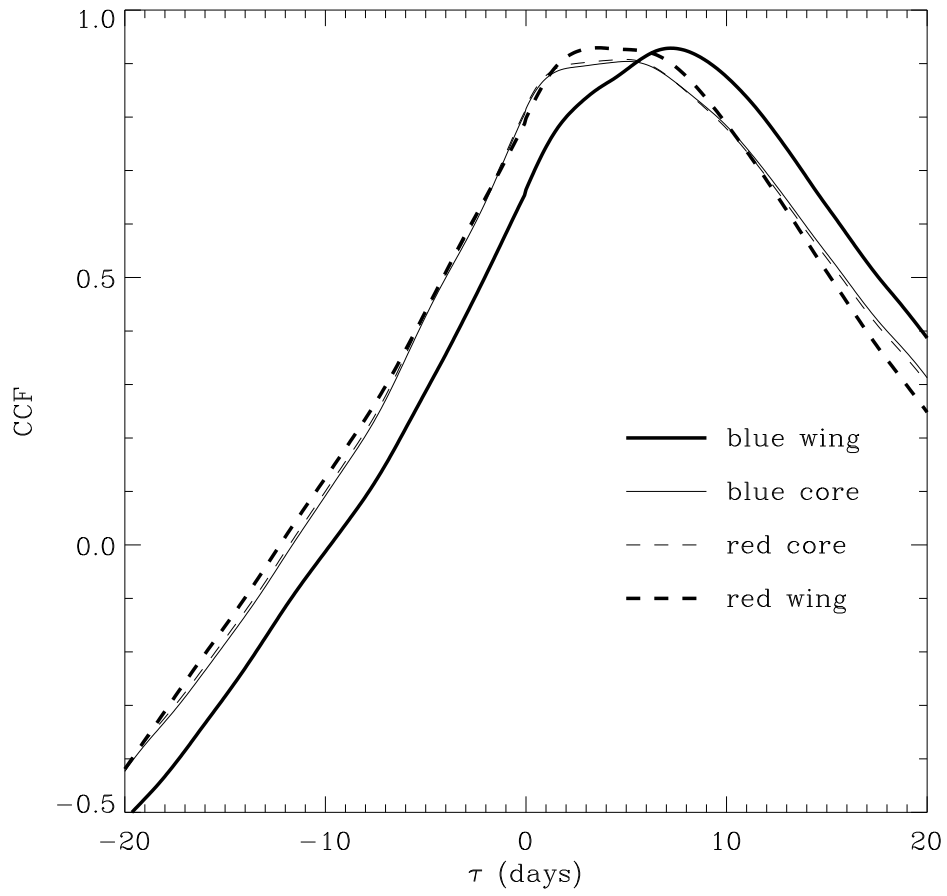


Figure 8